Ultrasound in Med. & Biol., Vol. 31, No. 11, pp. 1539–1550, 2005

0301-5629/05/$–see front matter

ELSEVIER

doi:10.1016/j.ultrasmedbio.2005.07.008

● *Original Contribution*

MINIATURIZED ULTRASOUND ARRAYS FOR INTERSTITIAL ABLATION AND IMAGING

INDER RAJ S. MAKIN,* T. DOUGLAS MAST,* WASEEM FAIDI,* MEGAN M. RUNK,* PETER G. BARTHE,† and MICHAEL H. SLAYTON†

*Ethicon Endo-Surgery, Cincinnati, OH, USA; and †Guided Therapy Systems, Mesa, AZ, USA

(*Received* 21 *December* 2004; *revised* 1 *July* 2005; *in final form* 7 *July* 2005)

Abstract—A potential alternative to extracorporeal, noninvasive HIFU therapy is minimally invasive intense ultrasound ablation that can be performed laparoscopically or percutaneously. An approach to minimally invasive ablation of soft tissue using miniaturized linear ultrasound arrays is presented here. Recently developed 32-element arrays with aperture 2.3 × 49 mm, therapy frequency 3.1 MHz, pulse-echo bandwidths >42% and surface acoustic energy density >80 W/cm^2, are described. These arrays are integrated into a probe assembly, including a coupling balloon and piercing tip, suitable for interstitial ablation. An integrated electronic control system allows therapy planning and automated treatment guided by real-time interstitial B-scan imaging. Image quality, challenging because of limited probe dimensions and channel count, is aided by signal processing techniques that improve image definition and contrast, resulting in image quality comparable to typical transabdominal ultrasound imaging. Ablation results from *ex vivo* and *in vivo* experiments on mammalian liver tissue show that this approach is capable of ablation rates and volumes relevant to clinical applications of soft tissue ablation such as treatment of liver cancer. (E-mail: i.makin@guidedtherapy.com) © **2005 World Federation for Ultrasound in Medicine & Biology.**

Key Words: **Ultrasound therapy, Thermal ablation, Surgery, Arrays, Liver cancer, Lesion monitoring.**

INTRODUCTION

Thermal ablation is increasingly becoming a viable alternative to surgical resection of pathologic soft tissues, including tumors of the liver and kidney. Available approaches include a number of interstitial radiofrequency ablation devices, which emit omnidirectional electromagnetic waves from antennae inserted into the tissue to be ablated; thermal coagulation is caused by the heating associated with the tissue's resistance to electrical current (Curley 2003; Zagoria 2003). Other interstitial thermal ablation devices employ microwave or laser radiation (Chin and Pautler 2002; Ogan and Caddedu 2002; Izzo 2003; Erce and Parks 2003). All of these methods can be deployed percutaneously, or within laparoscopic or open surgery procedures.

An alternative to minimally invasive ablation therapies is noninvasive ablation using extracorporeal high-intensity focused ultrasound (HIFU) (Kennedy et al. 2003). This approach has been investigated for a number of years (Fry 1958; Lele 1967) but has only recently resulted in clinical devices suitable for noninvasive ablation using extracorporeal (Wu et al. 2001; Kohrmann et al. 2002) and intracavitary (Gelet et al. 2000; Uchida et al. 2002) approaches. Current HIFU devices typically employ probes with one or more large focused, ultrasonic transducer elements for therapy and separate elements or arrays for B-scan imaging, which in some cases are integrated into the same probe as the therapy elements. In some systems, targeting and temperature monitoring are performed using magnetic resonance imaging (Chung et al. 1999; Stewart et al. 2003).

Each of these approaches has limitations. Minimally invasive, interstitial radiofrequency ablative methods, while favorable in cost, simplicity and procedure time, can require multiple insertions for larger tumors, thereby increasing their invasiveness and the risk of incomplete tumor ablation (Livraghi et al. 2003; de Baére et al. 2003). Although needle placement in these methods is usually guided by B-scan ultrasound imaging, treatment monitoring capability is limited because external ultrasound is strongly scattered and attenuated by bubbles formed throughout the region of thermal ablation. The

Address correspondence to: Inder Raj S. Makin, Guided Therapy Systems, 33 S. Sycamore St., Mesa, AZ, 85202, USA. E-mail: i.makin@guidedtherapy.com.

spatial extent of these bubbles does not, in general, correspond to the extent of the eventual ablation (Goldberg et al. 2000). All of these methods also have the disadvantage of poor selectivity, with little control over the ablation shape. HIFU, while attractive because of its noninvasive nature and high selectivity, is inherently slow because bulk ablation requires sweeping of a small focal region throughout the treatment volume (Wang et al. 2003). In addition, consistent treatment is made challenging by the severe focus aberration caused by propagation through the abdominal wall (Hinkelman et al. 1998). Because of this aberration, as well as other possible errors of orientation, spatial correspondence between imaged and treated locations can be uncertain in HIFU therapy. Use of MRI for guidance and temperature monitoring can improve the consistency of treatment (Chung et al. 1999; Stewart et al. 2003), but adds significant complication and expense while still requiring long procedure times.

The goal of the work presented here was to develop and test an ultrasound ablation device with the potential to overcome the limitations of both minimally invasive ablation methods and extracorporeal HIFU. Such a device would be capable of large ablation volumes within the treatment durations preferred by clinical practitioners, would allow precise selectivity to completely ablate tumors while sparing critical structures and would provide real-time image guidance during therapy. Our hypothesis was that these goals can be met by interstitial probes based on miniaturized dual-functionality (image and treat) ultrasound arrays (Barthe and Slayton 1999).

Interstitial transducers initially developed for intense ultrasound (IUS) therapy employed cylindrical elements for omnidirectional heating (Hynynen 1992; Jarosz 1996; Diederich et al. 1999). Use of planar (Chopra et al. 2000) or weakly focused (Lafon et al. 2002) elements with rotation allows more selective heating because of the directionality of ultrasound. Multiple-element arrays allow yet more selectivity by allowing switching (Deardorff and Diederich 2000) and limited focusing (Chopra et al. 2000). However, previous IUS devices have not allowed therapy and imaging to be performed using the same elements, which would be desirable because of precise colocation of imaging and treatment volumes.

In this paper, we present miniaturized array-based ultrasound probes designed for bulk interstitial ablation of soft tissue. The arrays are shown to be capable of high therapeutic ultrasound intensity (>80 W/cm^2 at the transducer face) as well as image quality comparable to diagnostic probes of similar frequency. These features allow successful bulk ablation of soft tissue with real-time B-scan imaging for treatment planning and monitoring.

MATERIALS AND METHODS

Array and electronics

The probe and system were designed to accomplish interstitial liver ablation. Design goals for ablation and imaging, based on standards set by current RF ablation devices (Curley 2003), were to enable a percutaneous approach for interstitial ablation, nominal ablation size of ~5 cm diameter, ablation rate ~2 mL/min and image resolution and contrast comparable to a transabdominal diagnostic ultrasound (3 to 5 MHz) curvilinear array. The approach taken here employed ultrasound arrays based on an acoustic stack design that provides both high power capabilities for therapy and broad bandwidth for imaging (Barthe and Slayton 1999).

To meet the required performance criteria, the probe therapy frequency was chosen to be 3.1 MHz and the array was designed with 32 elements, a 2.3 mm elevation and 1.53 mm pitch for an overall aperture of 49 mm. The relatively coarse array design (3.4 acoustic wavelengths at the nominal pulse-echo center frequency of 3.4 MHz) allowed the use of compact cabling suitable for use in a percutaneous probe, yet the channel count was considered sufficient to provide adequate image resolution as well as beam directivity suitable for uniform ablation of the target volume.

The array transducers employed were composed of a PZT-4 equivalent ceramic material diced into array elements, air-backed and bonded to a composite/epoxy matching layer. The probe housings were thin-walled, stainless steel or brass tubes of 3.3 mm outer diameter and 17 to 21 cm length, machined with a cut-out along the diameter to accept the transducer stack, which was carefully bonded to the tube and sealed at the periphery with epoxy. Array elements were electrically connected using a miniature flexible printed circuit that spanned the tube length. A representative array device is pictured in Fig. 1.

The probe design incorporating these arrays include a handle with a snap-in connector mating with the array's high-density interconnect board. The active array is contained within a 360° coupling balloon designed to allow $\pm$180° internal rotation of the transducer probe while the coupling balloon remains fixed. Balloons were constructed from 25 μm (0.001 in) thickness PET coupling balloon (Advanced Polymer, Salem, NH, USA) of 4.5 mm diameter, which was distally sealed in-house. The balloon assembly includes an in-flow port distal to the active array surface and a proximal out-flow port, allowing cooling of the array by forced flow of chilled water over the probe surface within the balloon. Water was chilled to 10°C to 15°C using a thermoelectric direct-to-air refrigeration system (Supercool DA-108, Goeteborg, Sweden) and peristaltically pumped (Cole-Parmer Mas-

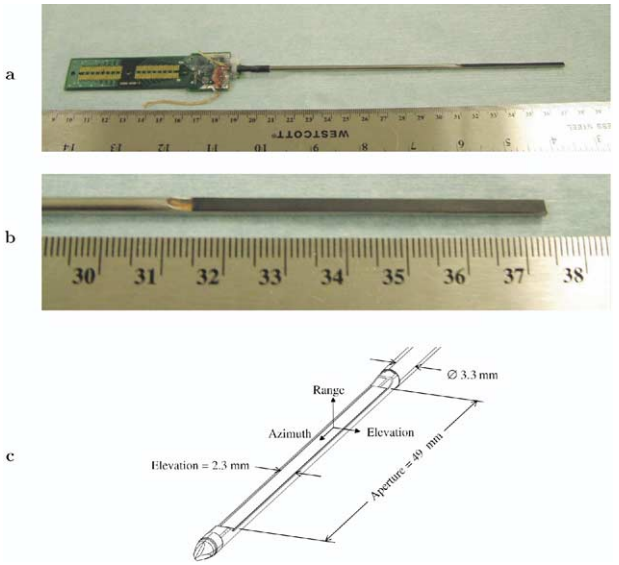

Fig. 1. Miniaturized image-treat array and probe. (a) Photograph of 3 mm probe with printed-circuit connector. (b) Closeup photograph of array face. (c) Sketch of probe configuration with piercing tip and coupling balloon.

terflex, Vernon Hills, IL, USA) through a closed-loop flow path at rates of 25 to 75 mL/min. The probe configuration, including the coupling balloon and tissue-piercing tip, are sketched in Fig. 1c.

The driving electronics for the system were composed of separate imaging and therapy modules, controlled by a host PC. The system electronics are pictured in Fig. 2. The system components, which include the Array Imaging Module, Array Therapy Module, host PC, and ultrasound probes, are illustrated by the block diagram shown in Fig. 3.

The Array Imaging Module provides imaging capabilities similar to current clinical imaging systems, including B-mode, M-mode and color Doppler imaging. Imaging controls, accessible by real-time user input and menu selections, include depth-dependent time-gain compensation, B-mode overall gain and transmit power, number and position of transmit focal zones, display depth, line density, and distance and area measurements. Analog beamforming performed by this module includes dynamic receive focusing with variable aperture size that allows the imaging f-number to be maintained constant for all image depths.

Imaging can be performed with dual mode imaging/therapy arrays or with standard diagnostic imaging probes, such as the 3.5 MHz transabdominal curved linear array and the 7 MHz laparoscopic linear array used for the imaging comparisons shown in the Results section. The same standard B-scan imaging techniques used for the diagnostic probes are also used for imaging using the miniaturized imaging-therapy arrays, with appropri-

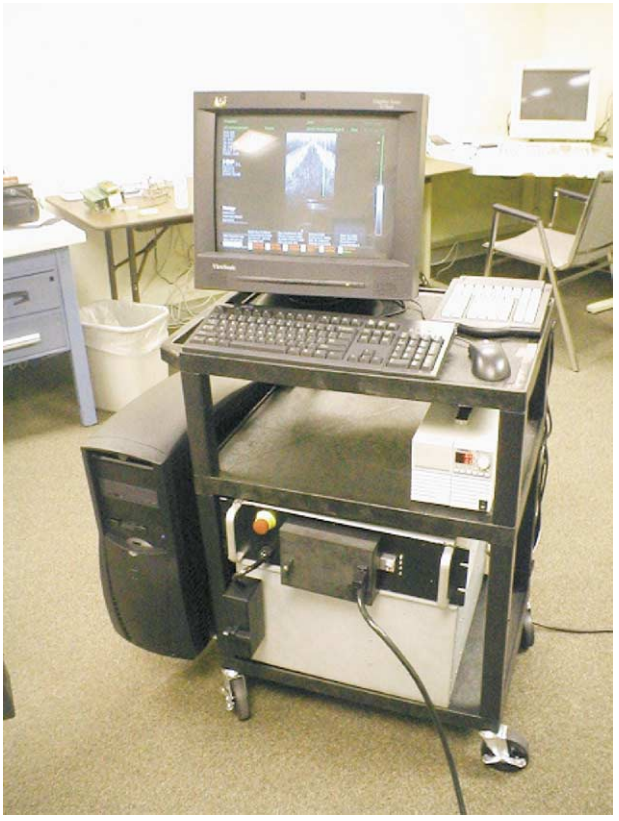

Fig. 2. Photograph of control system used with image-treat probes. Clockwise from bottom left: host PC; keyboard, monitor, command keypad and mouse; DC power supply; Array Imaging Module; Array Therapy Module. The B-scan shown on the monitor is of the reflecting cone used in power measurements.

ate adjustments for the apertures and numbers of elements employed. B-scan imaging can be performed at full frame rates (up to 200 fps, dependent on the imaging configuration employed) when the IUS ablation feature

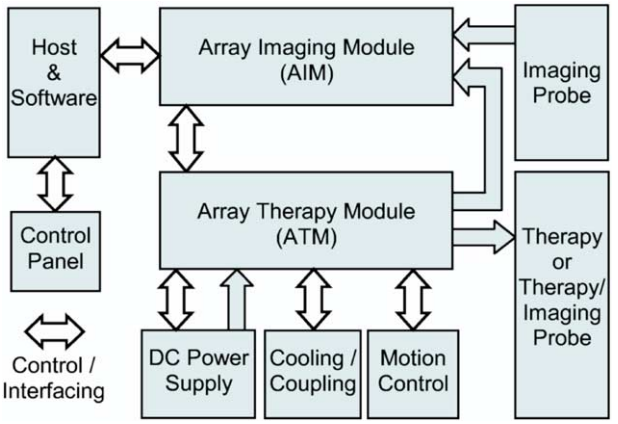

Fig. 3. Block diagram of controlling electronics for prototype ultrasound imaging-therapy system, showing system components and interfaces between modules.

is idle, including during the idle portion of each ablation duty cycle. During a therapy cycle, interleaved imaging is performed at a user-specified rate by rapid electronic switching between imaging and ablation modes. Beamformed radiofrequency A-line signals are available, together with synchronization trigger and clock signals, for each transmit focal zone of each image line.

The therapy module employed has 64 independent push-pull driver channels, each with a power capacity of 5 W. Drive amplitude is set using an electronically controlled DC power supply. Electrical matching circuits for each channel were tuned to maximize efficiency of the transmitted power at a nominal therapy frequency of 3 MHz. Further details of the system electronics are given by Barthe et al. (2004).

Pulse-echo performance was measured using a flat-plate reflector and pulsed excitation of individual array elements. Acoustic power performance was measured using a radiation force balance (Ultrasonic Power Meter UPM-DT-1 E, Ohmic Instruments, Easton, MD, USA) customized to accommodate insertion of the 49 mm side-firing array and the increased array output power.

Acoustic fields of the arrays were simulated using the Fresnel approximation for rectangular sources (Freedman 1960; Mast et al. 2005). Fields from individual elements with active dimensions of 1.5 × 2.3 mm, positioned with an interelement spacing of 0.0254 mm (0.001 in), were computed. The fields from each element were then coherently summed, using appropriate phase weighting corresponding to the phase discretization of the therapy module, at each field point. For comparison, fields were also measured using a Schlieren optical imaging system (OptiSon S-12 Ultrasound Beam Analyzer, Onda Corp, Sunnyvale, CA, USA) (Hanafy and Zanelli 1991).

B-scan imaging

Design goals for the imaging component of this research were to sufficiently delineate boundaries between normal and abnormal tissue, to achieve spatial and contrast resolution sufficient to identify critical structures in the vicinity of the target volume and to enable monitoring of the ablation process during treatment.

Enhanced B-scan images were formed by synchronously sampling the RF output of the imaging module at a rate of 33 MHz using an analog-to-digital converter board (Gage Compuscope 1450, Troy, NY, USA) housed in a separate PC. The digitized A-line signals were decimated to a sampling rate of 11 MHz, bandpass filtered to result in a center frequency of 4.0 MHz and a 17.5% bandwidth and coherently interpolated between adjacent signals to increase the effective line density.

In addition, an adaptive reverberation reduction method was employed to reduce signal artifacts. In this method, the artifactual portion of the echo signals was assumed to be the portion that changes very slowly from frame to frame, while the overall echo signals may change substantially (*e.g.*, due to tissue motion). This approach is effective in removing ringdown artifacts, caused mainly by the undamped metal housing, that depend only on the probe geometry and the electronic characteristics of each channel. Artifacts were estimated using a running weighted average defined by

$$B(y,z,T_i) \approx (1-\varepsilon)B(y,z,T_{i-1}) + \varepsilon p(y,z,T_i),$$

$$\varepsilon = \frac{\varepsilon_0}{2\pi}\cos^{-1} r\left[p_{i-1}, p_i\right], \quad (1)$$

where $p(y, z, t_i)$ is the ith frame of RF echo data, ε is a weighting factor determined from the cross-correlation r between a portion of two adjacent frames, and ε_0 is an user-definable coefficient less than unity. The estimated artifacts $B(y, z, T_i)$ were then digitally subtracted from the RF signals for each frame before envelope detection, logarithmic compression, scan conversion, smoothing and display.

Image quality of the prototype image-treat probes was measured using B-scan images of a standard quality assurance reference phantom (Model 539, ATS Laboratories, Bridgeport, CT, USA). Postprocessed (filtered, smoothed and reverberation-reduced as described above) images were obtained using three representative 32-element, 3 MHz, 3 mm arrays, all of which showed comparable results. Image quality metrics were determined using standard procedures recommended by the phantom manufacturer, based on objective criteria, including the distance between resolvable wires, the distinguishability of contrast cysts from the background and the minimum size anechoic cyst visible at a given depth.

Since existing procedures for liver ablation are guided using transabdominal imaging from standard diagnostic ultrasound systems, the imaging characteristics of the interstitial probes were compared with those of a standard transabdominal probe, using the same front end electronics. The transabdominal probe employed here was a 128-element curved linear array transducer designed for transabdominal imaging with a center frequency of 3.5 MHz. To mimic the situation of transabdominally guided intervention, a 30 mm depth absorbing standoff, made of the same urethane material as the phantom background, was employed.

Ablation

Ablation experiments using prototype image-treat probes were performed for a variety of *in vivo* and *in vitro* configurations. These experiments were initially designed to evaluate the ablation performance of the probes, including achievable ablation volumes, depths

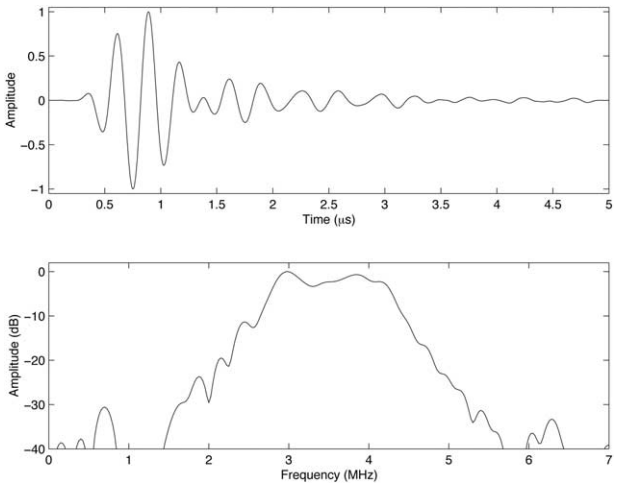

Fig. 4. Single-element pulse-echo waveform and spectrum for a representative miniaturized image-treat array.

and rates as well as the performance of B-scan imaging during ablation. Ablation configurations investigated included superficial exposures, with the probe positioned outside the treated organ, and interstitial exposures, with the probe inserted into the target tissue. In addition to stationary exposures, experiments with linear and rotational scanning of the probe assembly were performed.

In vitro ablation experiments were performed at room temperature in a water tank using excised bovine and porcine liver tissue. Transducer scanning was accomplished by a computer controlled positioning system (Velmex, Bloomfield, NY, USA). Before experiments, the water to be used was filtered and deionized (using a M2 Innovated Solutions (Wayne, PA, USA) filtration system with Liqui-Cel Extra-Flow Membrane Contractors) and degassed by a vacuum pump. *In vivo* ablation experiments were performed on anesthetized pigs after a laparotomy. During all ablation experiments, real-time B-scan images were acquired and recorded, with image acquisition occurring at maximum frame rate during the idle portion of each therapy cycle and at a reduced frame rate during the active portion of the cycle, accomplished by rapid switching between imaging and therapy modes of the controlling electronics. Delivered electrical power was monitored internally by the control electronics and displayed in real time.

Upon completion of each ablation experiment, tissue specimens were frozen overnight in preparation for sectioning. The samples were sliced into 1.5 to 4 mm sections using a standard meat slicer for evaluation. The ablation results were then characterized by ablation volume, ablation rate, continuous ablation depth and maximum ablation depth as follows. The area of damage on each slice was manually segmented based on visible discoloration of tissue and measured using commercial imaging software (Adobe Photoshop, San Jose, CA, USA). The total volume of the damaged zone was calculated using a summation of the areas of damage from each individual slice together with a measured average slice thickness. The maximum depth of the lesion was defined as the distance from the proximal tissue surface (or the insertion point in the case of interstitial ablation) to the deepest point of observable thermal damage in the tissue. The continuous depth of the lesion was defined as the depth from the tissue surface at which broad, contiguous thermal damage occurred.

RESULTS

Array performance

A typical pulse-echo waveform and spectrum for the miniaturized image-treat arrays, obtained from a single midarray element, is shown in Fig. 4. Based on the −6 dB points on the spectrum shown, the element response has a center frequency of 3.5 MHz and a bandwidth of 45%, sufficient to achieve the B-scan image quality illustrated below.

Example power measurements for uniform excitation of all 32 elements are shown in Fig. 5. The peak efficiency is associated with a resonance peak at about 3.1 MHz, which was chosen as the optimum therapy frequency for all measurements shown here. At 3.1 MHz, typical measured acoustic efficiencies were ~75% for a total acoustic output of 10 W (surface power density of 9 W/cm^2) and ~65% for a total acoustic output of 95 W (surface power density of 84 W/cm^2). Total acoustic power output of 100 W or greater is achievable using the probes and system described here.

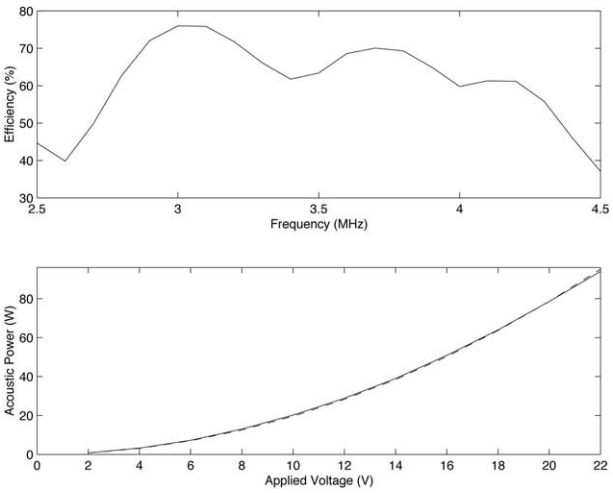

Fig. 5. Power performance for a representative miniaturized image-treat array. Top: acoustic efficiency vs. drive frequency. Bottom: acoustic power vs. applied voltage for simultaneous excitation of all 32 elements (solid line), parabolic fit (dashed line).

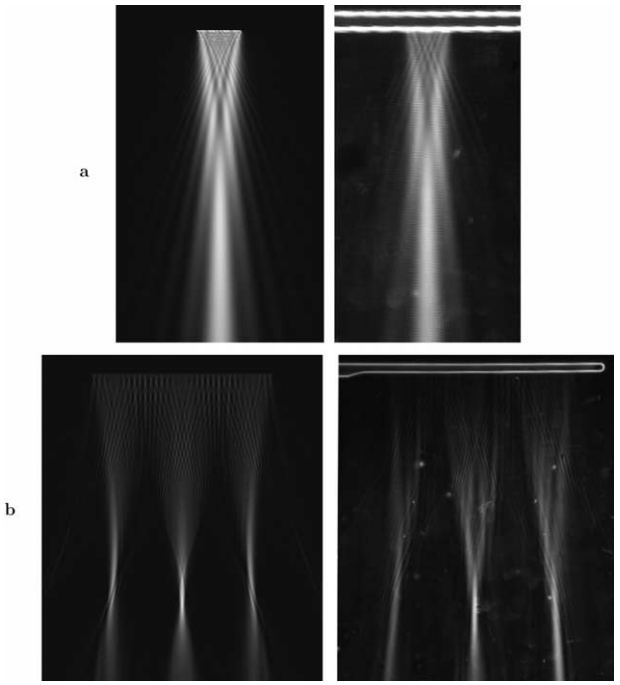

Fig. 6. Simulated and measured Schlieren images of acoustic fields from the miniaturized array. (a) Unfocused field of four adjacent elements. Each panel spans 28 mm in the horizontal (array) direction and 46 mm in the vertical (depth) direction. (b) Field of 32 elements electronically focused at a depth of 60 mm. Each panel spans 76 mm in the horizontal (array) direction and 88 mm in the vertical (depth) direction.

Simulated and measured fields for representative unfocused and electronically focused apertures are shown in Fig. 6. Visible details include nearfield interference and an amplitude peak at the near- farfield transition for the unfocused aperture as well as grating lobes for the focused aperture. These results illustrate that the miniaturized, 3 MHz array configuration is capable of forming directive beams as well as weak focusing, providing flexibility for design of bulk ablation methods.

B-scan imaging

For each probe, images of four regions of the ATS 539 reference phantom, demonstrating point resolution, contrast and functional resolution (*i.e.*, resolution of small anechoic structures) are depicted in Fig. 7. Image quality metrics, determined using the methods described above, are summarized in Table 1. Relative to the transabdominal probe, the 3 mm image-treat probe achieves superior point resolution in the azimuth (horizontal) direction, comparable point resolution in the range (vertical) direction and comparable contrast and functional resolution.

Interstitial images of a modified prostate phantom (CIRS Laboratories, Norfolk, VA, USA), mimicking an imaging configuration in which the probe is interstitially inserted into a tumor, are shown in Fig. 8 for a prototype 3 MHz, 3 mm image-treat probe as well as a standard 10 mm, 128 element laparoscopic imaging probe with a center frequency of 7 MHz (Vermon, Tours, Cedex, France). Finer speckle and better boundary definition are seen with the higher-frequency laparoscopic probe, consistent with its higher frequency and finer array pitch. However, both probes show comparable contrast differ-

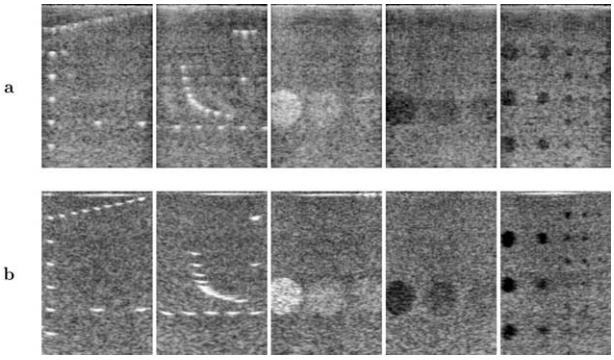

Fig. 7. B-scan images of a reference phantom. From left to right, the scattering objects imaged in each frame are nylon wires of 0.12 mm diameter (dead zone and vertical/horizontal resolution groups), cylindrical grayscale targets of diameter 15 mm (contrast 15 dB, 6 dB, 3 dB, −15 dB, −6 dB and −3 dB relative to background) and cylindrical anechoic cysts (diameter 8 mm, 6 mm, 4 mm, 3 mm and 2 mm). Each panel shows an image area of 48 mm horizontally and 71 mm vertically. (a) Miniaturized image-treat probe. (b) Transabdominal curved linear array probe.

Table 1. Image quality metrics for a 3 MHz, 3 mm image-treat array and a reference 3.5 MHz curved linear array used with a 30 mm standoff mimicking a transabdominal imaging configuration. Point resolution is based on the smallest distance between resolvable wires, contrast resolution is based on the visibility of grayscale targets against the speckle background and functional resolution based on the smallest resolvable anechoic target. In each case, smaller metrics correspond to better performance.

Metric	Image-treat array	Transabdominal array
Axial point resolution at 30 mm depth (mm)	2	2
Azimuthal point resolution at 40 mm depth (mm)	2	5
Contrast resolution at 50 mm depth (dB)	3	3
Functional resolution at 20 mm depth (mm)	4	3
Functional resolution at 40 mm depth (mm)	4	6
Functional resolution at 60 mm depth (mm)	4	6

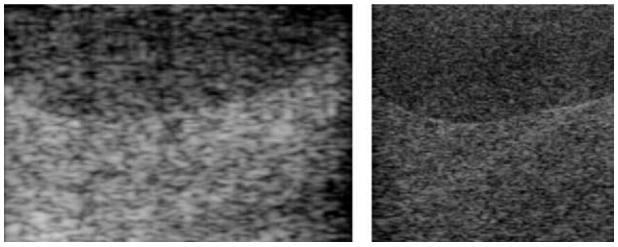

Fig. 8. Interstitial B-scan images of a tumor phantom. Left: miniaturized image-treat probe, center frequency 3.5 MHz. Right: laparoscopic imaging probe, center frequency 7 MHz. The horizontal (array direction) range shown is 49 mm for the left panel and 34 mm for the right panel, while the vertical (depth) range shown is 34 mm for both panels.

ences between the tumor-mimicking and background regions, suggesting that the 3 MHz image-treat probes are sufficiently capable to distinguish tissue boundaries relevant to ablation procedures.

Ablation

Series of ablation experiments performed using the 3 MHz image-treat probes have included *in vitro* exposures on *ex vivo* bovine and porcine liver tissue specimens (95 single exposures from the tissue surface, 41 surface scans and 53 interstitial exposures) as well as *in vivo* exposures in 14 open surgical procedures in pig liver (22 single exposures, 3 surface scans and 30 interstitial exposures). Retrospective statistical analysis on the measured ablation results for single, stationary exposures shows some trends of *in vivo* and *in vitro* bulk ablation that are consistent with modeling results (Mast et al. 2005), as described below. For scanned exposures *in vivo* and *ex vivo* employing acoustic intensities of 60 to 80 W/cm^2 at the array surface, typical ablation rates were on the order of 2 mL/min and depths of maximum ablation (distance from the active array surface) were typically on the order of 30 mm. Maximum ablation rates achieved were $>$4 ml/min both *in vivo* and *in vitro*. Maximum ablation depths achieved were $>$35 mm for *in vitro* exposures and $>$45 mm for *in vivo* exposures.

To illustrate the effect of exposure conditions on bulk liver ablation, retrospective linear regression analysis was performed for all available *in vivo* and *in vitro* stationary, superficial ablation experiments using the 3 MHz, 3 mm image-treat arrays. Experiments were excluded from this analysis if exposures were performed at multiple locations, if ablation volume and depth were not quantitatively measured or if vascular clamping (Pringle maneuver) was employed to reduce perfusion effects *in vivo*. The variety of scanning conditions employed in these exploratory experiments is not amenable to quantitative statistical analysis for scanned ablation experiments. In the analyses, performed on stationary, superficial exposure results, measured values for volumetric ablation rate and maximum ablation depth, determined as described in the Materials and Methods section, were used as dependent variables, while time-averaged acoustic power and time-averaged surface intensity (defined as time-averaged acoustic power divided by the active aperture area) were used as independent variables. Scatter plots of these variables are shown in Fig. 9.

Regression results are given in Table 2. Implications of the regression results include a strong correlation between delivered acoustic power and ablation rate, which is expected based on straightforward energy considerations (Mast et al. 2005). Also notable is that ablation rate and volume correlate more highly with acoustic power for *in vitro* exposures, but correlate more highly with surface intensity for *in vivo* exposures. The probable reason for this difference is that heat losses from perfusion cause greater local energy density to be required for *in vivo* ablation. Fig. 9 shows plots of ablation rate vs. average acoustic power and maximum ablation depth vs. average surface intensity for the stationary *in vitro* and *in vivo* experiments. These plots illustrate the greater variability and larger energy requirements for *in vivo* ablation, both of which are influenced by tissue motion and inhomogeneous perfusion. Also notable is the absence of *in vivo* ablation below particular power and intensity thresholds, which is consistent with analytic and simulated results (Mast et al. 2005).

Examples of ablation performed with the image-treat arrays are shown in Fig. 10, Fig. 11 and Fig. 12. The stationary, superficial exposure illustrated in Fig. 10 was performed on excised porcine liver tissue. The array was placed in a coupling balloon and positioned approximately 2 mm from the tissue surface. A 3 mm, 32 element image-treat array was fired at 3.1 MHz with an active aperture of 24 elements (active aperture size 2.3 $\times$ 37 mm) and instantaneous acoustic power of 60.3 W, corresponding to a surface acoustic intensity of 71.7 W/cm^2, using an 86% duty cycle (4.3 s on, 0.7 s off). All elements were fired in phase, so that heat deposition occurred within a collimated beam. After a 2 min treatment, a volume of 5.6 mL was thermally damaged, so that the ablation rate was 2.8 mL/min. The measured continuous depth of lesioning was 23 mm while the maximum depth was 36 mm. A 3D volume reconstruction of the thermal lesion, obtained by sequential stacking of manually drawn lesion boundaries for each cross section (SURFdriver 3.5.6), shows how the lesion tapers with depth.

The lesion volume shown in Fig. 11 was created in excised bovine liver tissue using a repetitive linear scan technique. The array was placed in a polyester coupling balloon with chilled water flowing for cooling and posi-

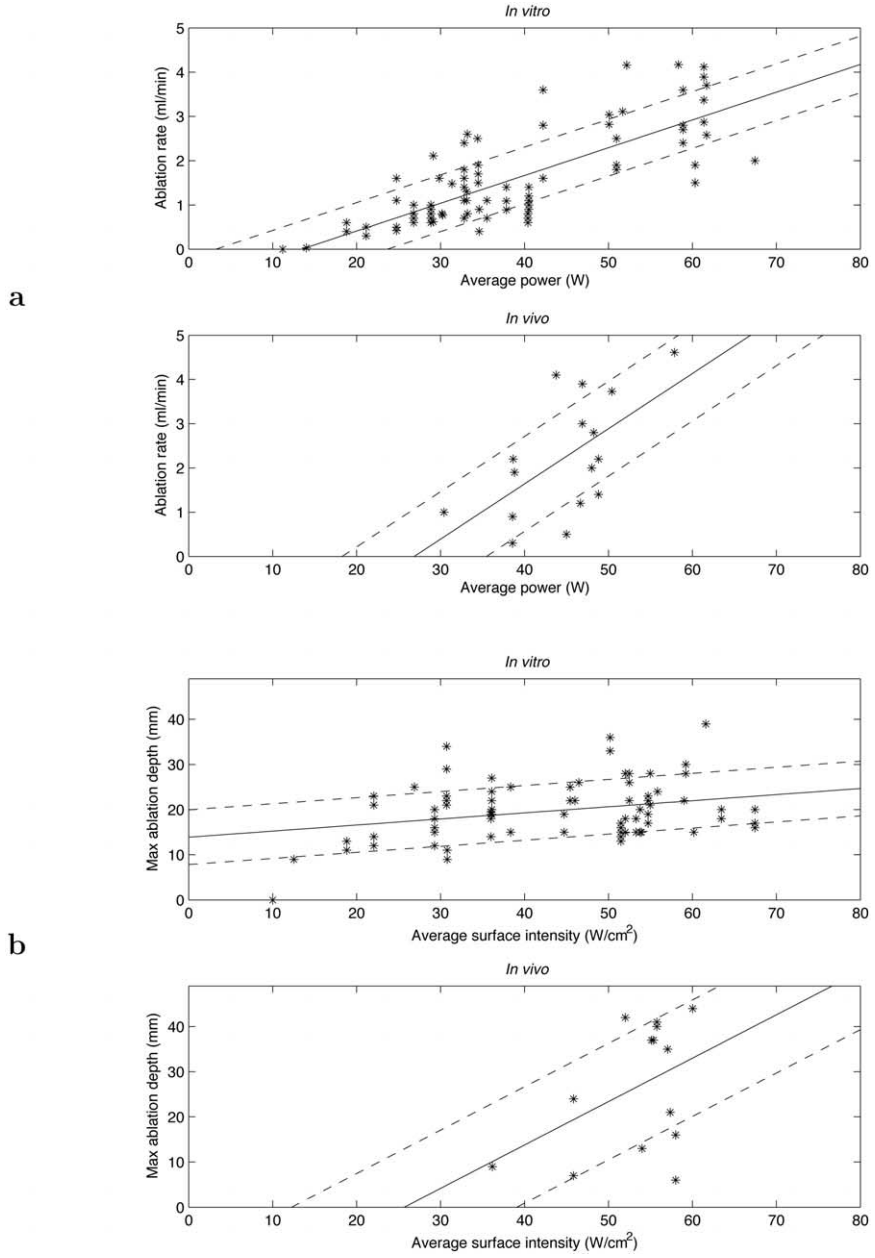

Fig. 9. Dependence of ablation performance on exposure conditions for stationary, superficial *in vitro* and *in vivo* ablation experiments. Each plot shows a line of best fit and lines at ± one standard deviation from best fit, together with data points for each individual experiment. Fit parameters are given in Table 2. (a) Ablation rate vs. time-averaged acoustic power during the experiment. (b) Maximum ablation depth vs. time-averaged acoustic intensity at the array surface.

tioned 5 to 10 mm from the tissue surface. All 32 array elements (active aperture 2.3 × 49 mm) were simultaneously fired in phase at 3.1 MHz with an acoustic power of 75.6 W, corresponding to a surface source intensity of 67.4 W/cm^2, in 2 s pulses with an 80% duty cycle. At the same time, the array was asynchronously scanned in one direction over a range of 53 mm, with a dwell time of 2 s at steps separated by 1 mm, and repositioned at its initial location after each scan. Fourteen scans were performed sequentially for a total treatment duration of 29 min. The treated tissue volume in this case was 94.2 mL, so that the ablation rate was 3.3 mL/min. The treated volume was continuous to a 31 mm depth and the maximum depth of any ablation was 37 mm.

For the *in vivo* scanned treatment illustrated in Fig. 12, a 32 element, 3 mm image-treat array was

Table 2. Linear regression statistics for single, stationary ablation experiments. Ablation rate and maximum ablation depth are related to the time-averaged acoustic power and time-averaged acoustic intensity at the probe surface. Shown are the least-mean-square-error fits for slope and intercept, correlation coefficient between the variable pairs, standard deviation of the slope, the *p*-value of the fit or the probability of each fit occurring by chance for the given number of experiments *N*.

	Regression vs. average acoustic power (W)					
	N	Slope	Intercept	Corr. coef.	St. dev.	*p*
In vitro rate (ml/min)	95	0.063	−0.86	0.78	0.65	$2.3 \cdot 10^{-14}$
In vitro depth (mm)	93	0.20	12.2	0.41	5.8	$7.1 \cdot 10^{-5}$
In vivo rate (ml/min)	16	0.12	−3.4	0.60	1.1	0.016
In vivo depth (mm)	14	0.65	−1.8	0.26	13.8	0.32
	Regression vs. average surface intensity (W/cm^2)					
	N	Slope	Intercept	Corr. coef.	St. dev.	*p*
In vitro rate (ml/min)	95	0.024	0.42	0.31	0.99	$2.8 \cdot 10^{-3}$
In vitro depth (mm)	93	0.13	13.9	0.28	6.1	$7.0 \cdot 10^{-3}$
In vivo rate (ml/min)	16	0.12	−4.1	0.62	1.1	0.014
In vivo depth (mm)	14	0.96	−24.7	0.44	12.9	0.10

inserted interstitially into the medial lobe of a porcine liver during an open surgical procedure. All 32 array elements were fired in phase at 3.1 MHz with an acoustic power 66.7 W (source intensity of 59.5 W/cm^2) in 5 s pulses with an 80% duty cycle. A 45° rotational scan was produced in four 1.5 min treatments, with the array fixture manually rotated by 15° between steps. The resulting ablation volume was measured to be 8.9 mL, corresponding to a 1.4 mL/min ablation rate. The continuous depth of the lesion, which includes areas of coagulated tissue not seen in *ex vivo* exposures, was 16 mm and the maximum depth of the lesion was 24 mm. Also notable in Fig. 12 is a region of reduced treatment in the vicinity of a large blood vessel, illustrating the challenges posed by perfusion *in vivo*.

B-scan images taken using a 3 MHz, 3 mm image-treat probe during an *in vivo* interstitial ablation experiment are shown in Fig. 13. The pretreatment image shows resolution of liver structure including a large vessel. Typical effects of ablation on B-scan images are

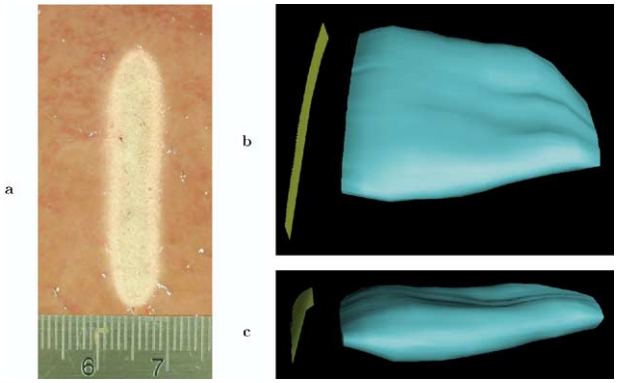

Fig. 10. Lesion from an *ex vivo* stationary exposure. (a) Cross section parallel to the probe surface at a depth of 7 mm. (b) Oblique view showing probe orientation and lesion extent in the array direction. (c) Oblique view showing probe orientation and lesion extent in the elevation direction. The maximum lesion depth is 36 mm.

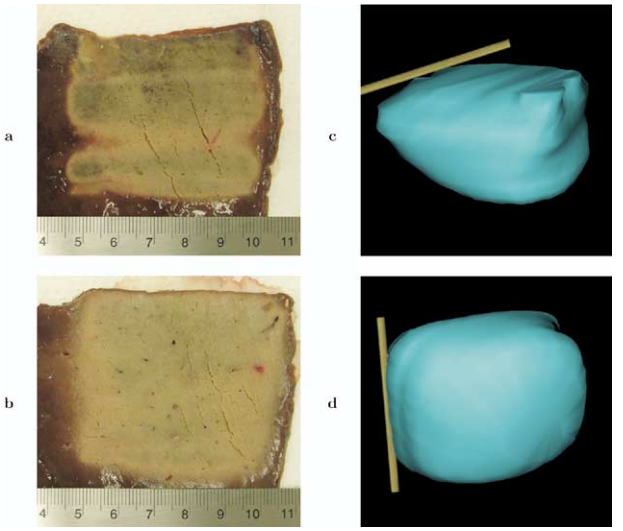

Fig. 11. Lesion from an *ex vivo* linear-scan exposure. (a) Cross section at 3.1 mm depth. The probe scan direction is from left to right. (b) Cross section at 12.4 mm depth. (c) 3D surface reconstruction of entire lesion from multiple cross sections, oblique view showing tissue surface and probe orientation at the starting point of the linear scan. (d) 3D reconstruction, distal view.

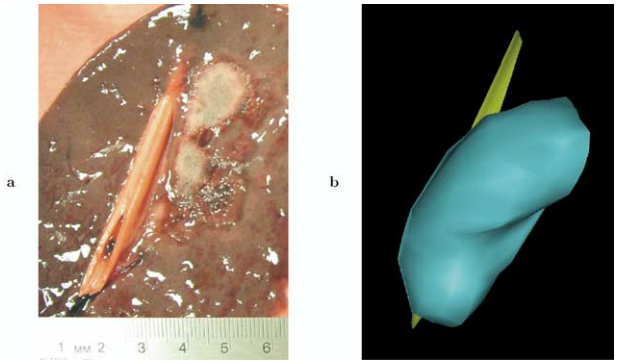

Fig. 12. Lesion from an *in vivo* interstitial, rotationally scanned exposure. (a) Cross section approximately along the probe track. (b) Surface rendering of reconstructed lesion.

shown in the following two panels. The second panel shows a hyperechoic spot immediately after its spontaneous formation about 60 s after the beginning of treatment. The third panel shows the hyperechoic spot after about 80 s treatment, at which time the proximal portion of the image is dominated by the hyperechoic spot.

DISCUSSION

The research reported here was conducted to develop ultrasound based tools for management of liver tumors using a percutaneous approach. Design criteria were based on the concept of a miniaturized (~3 mm outer diameter) probe that can be inserted within a tumor and ablate a tissue mass of 1 to 5 cm diameter. The approach is very similar to existing RF-based techniques for liver ablation. However, ablation using intense ultrasound has several potential advantages over other thermal ablation techniques. Compared to other interstitial ablation modalities for liver, the ultrasonic ablation approach offers the user greater treatment selectivity because of the directivity of ultrasound. In addition, the integration of imaging and treatment modalities in a single device offers further advantages.

The present approach, employing miniaturized image-treat ultrasound arrays, enables the user to scan and identify the tumor boundary using the same transducer elements employed for ablation, ensuring accurate targeting. An ablation protocol can then be programmed after considering the location of any critical structures. During ablation, the probe and control electronics can switch between imaging and therapy modes, so that the treatment plane is imaged in real time, potentially providing better predictability of tissue ablation.

Image quality achieved using these probes is comparable to that for typical transabdominal imaging configurations used in guidance of other interstitial ablation procedures. The image quality achieved with the present interstitial probes is limited by design constraints for their application; for example, a 3 mm package suitable for interstitial deployment requires an element elevation dimension of about 2 mm, cable sizes for high-power delivery limit the possible number of channels and the large aperture needed for bulk ablation applications requires a coarse array pitch. However, imaging using these probes is not intended to be diagnostic, but is designed for better planning and monitoring of therapy. For this purpose, the complete coregistration of imaging and treatment volumes is a significant advantage. The miniaturized image-treat probes presented here should be adequate to detect boundaries between normal and abnormal tissue, as well as to monitor ablation procedures.

Monitoring of ablation procedures with B-scan imaging is most straightforwardly performed by observation of hyperechoic regions associated with gas activity, such as those illustrated in Fig. 13, similar to those appearing on B-scans during radiofrequency ablation procedures (Goldberg 2000). Although some gas activity may be associated with inertial cavitation, the primary cause in the experiments reported here is believed to be tissue boiling, due to the delayed onset of hyperechoic spots, and the observation that increased B-scan brightness consistently corresponded with significant thermal lesioning. However, the spatial extent of hyperechoic spots was found not to correspond precisely with the extent of significant tissue coagulation. Correspondence between lesioned and hyperechoic regions is problematic, particularly in the depth direction, in part because the depth of hyperechoic spots can be artifactually reduced by increased attenuation, or conversely, increased by acoustic reverberation and bubble resonance.

Gas activity caused by tissue heating also limits the achievable depth of ablation due to corresponding increases in attenuation. Methods of ablation that minimize proximal preheating, such as the continuous-sweep method used for the experiment illustrated by Fig. 11,

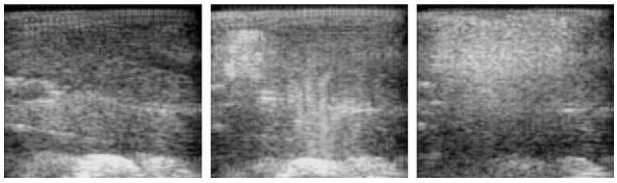

Fig. 13. B-scan images from an *in vivo* interstitial ablation experiment, with a 3 mm image-treat probe inserted interstitially into normal porcine liver. Each panel spans 49 mm in the horizontal (array) direction and 43 mm in the vertical (depth) direction. From left to right: pretreatment image showing resolution of a large vessel (upper right) and other tissue structure; image after 60 s treatment, showing a hyperechoic region; image after 80 s treatment, showing a larger hyperechoic region.

can allow increased ablation depth by delaying the shadowing effects caused by gas bubbles. Further discussion of this issue, illustrated by simulated and experimental results, is given elsewhere (Mast et al. 2005).

Since local heat deposition in bulk ultrasound ablation occurs more slowly than in HIFU treatments, bulk treatments are more susceptible to perfusion losses. Certain exposure conditions, such as those employing relatively long exposure times with relatively low acoustic energy density, may produce significant lesioning in *in vitro* experiments but fail to produce lesioning *in vivo*. This effect is analyzed for the present bulk ablation methods in a companion paper (Mast et al. 2005). However, bulk ablation *in vivo* can also be performed using relatively low energy densities when vascular occlusion methods such as the Pringle maneuver are employed. These methods of vascular occlusion, which is currently employed for radiofrequency ablation in some open and laparoscopic surgical procedures, have proven successful in increasing the quantity and reliability of thermal ablation (Burdio et al. 2003; de Baére et al. 2003).

In addition, a significant challenge for practical bulk ablation *in vivo* using intense ultrasound is variability due to unknown perfusion losses, particularly inhomogeneous losses associated with larger blood vessels. Resolution of this problem may require methods of continuously monitoring tissue ablation so that treatment parameters can be appropriately modified to achieve the desired endpoint. This form of treatment control may be achievable using MRI-based temperature monitoring, with correspondingly increased treatment cost and complexity (Chung et al. 1999; Stewart et al. 2003); monitoring using appropriate processing of pulse-echo ultrasound from image-treat arrays also shows promise (Makin et al. 2004).

CONCLUSIONS

The design, implementation and results from prototype array-based, dual-modality (image and treat) ultrasound systems for interstitial bulk tissue ablation and imaging have been described. This system, which includes a probe assembly allowing transducer cooling and rotation, has been shown to be capable of high rates of tissue ablation (up to ~3 mL/min). The results indicate that these systems are capable of bulk ablation of soft tissue comparable to existing interstitial ablation techniques used clinically for liver ablation, but with the potential advantages of increased treatment selectivity and control. Image quality achieved using these image-treat probes is comparable to imaging from standard transabdominal imaging probes. Real-time B-scan imaging with identical colocation of treatment and image volumes is available during the entire ablation procedure, with potential benefits for therapy planning, monitoring and evaluation. These results suggest that intense ultrasound therapy using image-treat arrays is a viable method for bulk ablation of soft tissue.

REFERENCES

Barthe PG, Slayton MH. Efficient wideband linear arrays for imaging and therapy. IEEE Ultrasonics Symposium 1999;1249–1252.

Barthe PG, Slayton MH, Jaeger PM, Makin IRS, Gallagher LA, Mast TD, Runk MM, Faidi W. Ultrasound therapy system and ablation results utilizing miniature imaging/therapy arrays. IEEE Ultrasonics Symposium 2004.

Burdio F, Guemes A, Burdio JM, et al. Large hepatic ablation with bipolar saline-enhanced radiofrequency: An experimental study in *in vivo* porcine liver with a novel approach. J Surg Res 2003;110: 193–201.

Chin JL, Pautler SE. New technologies for ablation of small renal tumors: Current status. Can J Urol 2002;9:1576–1582.

Chopra R, Bronskill MJ, Foster FS. Feasibility of linear arrays for interstitial ultrasound thermal therapy. Med Phys 2000;27:1281–1286.

Chopra R, Luginbuhl C, Weymouth AJ, Foster FS, Bronskill MJ. Interstitial ultrasound heating applicator for MR-guided thermal therapy. Phys Med Biol 2001;46:3133–3145.

Chung AH, Jolesz FA, Hynynen K, Thermal dosimetry of a focused ultrasound beam *in vivo* by magnetic resonance imaging. Med Phys 1999;26:2017–2026.

Curley SA. Radiofrequency ablation of malignant liver tumors. Ann Surg Oncol 2003;10:338–347.

Deardorff DL, Diederich CJ. Axial control of thermal coagulation using a multi-element interstitial ultrasound applicator with internal cooling. IEEE Trans Ultrason Ferroelectr Freq Control 2000;47: 170–178.

de Baére T, Risse O, Kuoch V, et al. Adverse effects during radiofrequency treatment of 582 hepatic tumors. Am J Roentgenol 2003; 181:695–700.

Diederich CF, Nau WH, Stauffer PR. Ultrasound applicators for interstitial thermal coagulation. IEEE Trans Ultrason Ferroelectr Freq Control 1999;46:1218–1228.

Erce C, Parks RW. Interstitial ablative techniques for hepatic tumors. Br J Surg 2003;90:272–289.

Freedman A. Sound field of a rectangular piston. J Acoust Soc Am 1960;32:197–209.

Fry WJ. Biological and medical acoustics. J Acoust Soc Am 1958;30: 387–393.

Gelet A, Chapelon JY, Bouvier R, et al. Transrectal high-intensity focused ultrasound: Minimally invasive therapy of localized prostate cancer. J Endourol 2000;14:519–528.

Goldberg SN, Gazelle GS, Mueller PR. Thermal ablation therapy for focal malignancy: A unified approach to underlying principles, techniques, and diagnostic imaging guidance. Am J Roentgenol 2000;174:323–331.

Hanafy A, Zanelli C, Quantitative real-time pulsed Schlieren imaging of ultrasonic waves. IEEE Ultrasonics Symposium 1991;1223–1227.

Hinkelman LM, Mast TD, Metlay LA, Waag RC. The effect of abdominal wall morphology on ultrasonic pulse distortion. Part I: Measurements. J Acoust Soc Am 1998;104:3635–3649.

Hynynen K. The feasibility of interstitial ultrasound hyperthermia. Med Phys 1992;19:979–987.

Izzo F. Other thermal ablation techniques: Microwave and interstitial ablation of liver tumors. Ann Surg Oncol 2003;10:491–497.

Jarosz BJ. Feasibility of ultrasound hyperthermia with waveguide interstitial applicator. IEEE Trans Biomed Eng 1996;43(11):1106–1115.

Kennedy JE, ter Haar GR, Cranston D. High intensity focused ultrasound: Surgery of the future? Br J Radiol 2003;76:590–599.

Kohrmann KU, Michel MS, Gaa J, Marlinghaus E, Alken P. High intensity focused ultrasound as noninvasive therapy for multilocal renal cell carcinoma: Case study and review of the literature. J Urol 2002;167:2397–2403.

Lafon C, de Lima DM, Theillière Y, Prat F, Chapelon JY, Cathignol D. Optimizing the shape of ultrasound transducers for interstitial thermal ablation. Med Phys 2002;29:290–297.

Lele PP. Production of deep focal lesions by focused ultrasound–current status. Ultrasonics 1967;5:105–112.

Livraghi T, Solbiati L, Meloni MF, Gazelle GS, Halpern EF, Goldberg SN. Treatment of focal liver tumors with percutaneous radiofrequency ablation: Complications encountered in a multicenter study. Radiology 2003;226:441–451.

Makin IRS, Mast TD, Faidi W, Runk MM, Barthe PG, Slayton MH. B-scan imaging and thermal lesion monitoring using miniaturized dual-functionality ultrasound arrays. IEEE Ultrasonics Symposium 2004.

Mast TD, Makin IRS, Faidi W, Runk MM, Barthe PG, Slayton MH. Bulk ablation of soft tissue with intense ultrasound: Modeling and experiments. J Acoust Soc Am. 2005;118 (in press).

Ogan K, Cadeddu JA. Minimally invasive management of the small renal tumor: Review of laparoscopic partial nephrectomy and ablative techniques. J Endourol 2002;16:635–43.

Stewart EA, Gedroyc WMW, Tempany CMC, et al. Focused ultrasound treatment of uterine fibroid tumors: Safety and feasibility of a noninvasive thermoablative technique. Am J Obstet Gynecol 2003;189:48–54.

Uchida T, Sanghvi NT, Gardner TA, et al. Transrectal high-intensity focused ultrasound for treatment of patients with stage T1b-2n0m0 localized prostate cancer: A preliminary report. Urology 2002;59:394–398.

Wang Z, Bai J, Li F, et al. Study of a "biological focal region" of high-intensity focused ultrasound. Ultrasound Med Biol 2003;29:749–754.

Wu F, Chen WZ, Bai J, et al. Pathological changes in human malignant carcinoma treated with high-intensity focused ultrasound. Ultrasound Med Biol 2001;27:1099–1106.

Zagoria RJ. Percutaneous image-guided radiofrequency ablation of renal malignancies. Radiol Clin North Am 2003;41:1067–1075.